5 Hyperspectral Data Processing Algorithms

Antonio Plaza, Javier Plaza, Gabriel Martín, and Sergio Sánchez

CONTENTS

5.1 INTRODUCTION

Hyperspectral imaging is concerned with the measurement, analysis, and interpretation of spectra acquired from a given scene (or specific object) at a short, medium, or long distance by an airborne or satellite sensor [1]. The concept of hyperspectral imaging originated at NASA's Jet Propulsion Laboratory in California with the development of the Airborne visible infrared imaging spectrometer (AVIRIS), able to cover the wavelength region from 400 to 2500 nm using more than 200 spectral channels, at nominal spectral resolution of 10 nm [2]. As a result, each pixel vector collected by a hyperspectral instrument can be seen as a *spectral signature* or *fingerprint* of the underlying materials within the pixel.

The special characteristics of hyperspectral data sets pose different processing problems [3], which must be necessarily tackled under specific mathematical formalisms, such as classification, segmentation, image coding, or spectral mixture analysis [4]. These problems also require specific dedicated processing software and hardware platforms. In most studies, techniques are divided into full-pixel and mixed-pixel techniques, where each pixel vector defines a *spectral signature* or *fingerprint* that uniquely characterizes the underlying materials at each site in a scene [5]. Mostly based on previous efforts in multispectral imaging, full-pixel techniques assume that each pixel vector measures the response of one single underlying material. Often, however, this is not a realistic assumption. If the spatial resolution of the sensor is not fine enough to separate different pure signature classes at a macroscopic level, these can jointly occupy a single pixel, and the resulting spectral signature will be a composite of the individual pure spectra, called *endmembers* in hyperspectral terminology [6]. Mixed pixels can also result when distinct materials are combined into a homogeneous or intimate mixture, which occurs independently of the spatial resolution of the sensor.

To address these issues, spectral unmixing approaches have been developed under the assumption that each pixel vector measures the response of multiple underlying materials [7].

Our main goal in this chapter is to provide a seminal view on recent advances in techniques for full-pixel and mixed-pixel processing of hyperspectral images, taking into account both the spectral and spatial properties of the data. Due to the small number of training samples and the high number of features available in remote sensing applications, reliable estimation of statistical class parameters is a challenging goal [4]. As a result, with a limited training set, classification accuracy (in full-pixel sense) tends to decrease as the number of features increases. This is known as the Hughes effect. Furthermore, high-dimensional spaces are mostly empty, thus making density estimation more difficult. One possible approach to handle the problem of dimensionality is to consider the geometrical properties rather than the statistical properties of the classes. In this regard, it is important to develop techniques able to select the most highly informative training samples from the available training set [8]. The good classification performance already demonstrated by techniques such as kernel methods and support vector machines (SVMs) in remote sensing applications [9], using spectral signatures as input features, has been further increased using intelligent training sample selection algorithms [10].

It should be noted that most available hyperspectral data processing techniques (including both full-pixel and mixed-pixel techniques) focused on analyzing the data without incorporating information on the spatially adjacent data, that is, hyperspectral data are usually not treated as images, but as unordered listings of spectral measurements with no particular spatial arrangement. In certain applications, however, the incorporation of spatial and spectral information is mandatory to achieve sufficiently accurate mapping and/or classification results [11–13]. To address the need for developments able to exploit a priori information about the spatial arrangement of the objects in the scene in order to complement spectral information, this chapter also presents several techniques for spatial–spectral data processing in the context of a mixed-pixel classification scenario.

5.2 SUPPORT VECTOR MACHINES

Supervised classification is one of the most commonly undertaken analyses of remotely sensed hyperspectral data. The output of a supervised classification is effectively a thematic map that provides a snapshot representation of the spatial distribution of a particular theme of interest such as land cover. Recent research has indicated the considerable potential of SVM-based approaches for the supervised classification of remotely sensed hyperspectral data [14]. Comparative studies have shown that classification by an SVM can be more accurate than techniques such as neural networks, decision trees, and probabilistic classifiers such as maximum likelihood classification [9]. This is due to the superior performance of SVMs when analyzing high-dimensional data (particularly in the presence of limited training samples), which generally results in higher relative accuracies than those reported for other classification methods. SVMs were designed for binary classification but various methods exist to extend the binary approach to multiclass classification, such as the *one versus the rest* and the *one versus one* strategies [15].

In essence, the SVM classification is based on fitting an optimal separating hyperplane between classes by focusing on the training samples that lie at the edge of the class distributions, which are the support vectors (Figure 5.1, reproduced from [9]). All of the other training samples are effectively discarded as they do not contribute to the estimation of hyperplane location. In this way not only is an optimal hyperplane fitted, in the sense that it is expected to be generalizable to a large degree, but also a high accuracy may be obtained with the use of a small training set. It should be noted that the SVM used with a kernel function is a nonlinear classifier, where the nonlinear ability is included in the kernel. Different kernels lead to different SVMs. The most used kernels are the polynomial kernel, the Gaussian kernel, or the spectral angle mapper kernel, among many others [9].

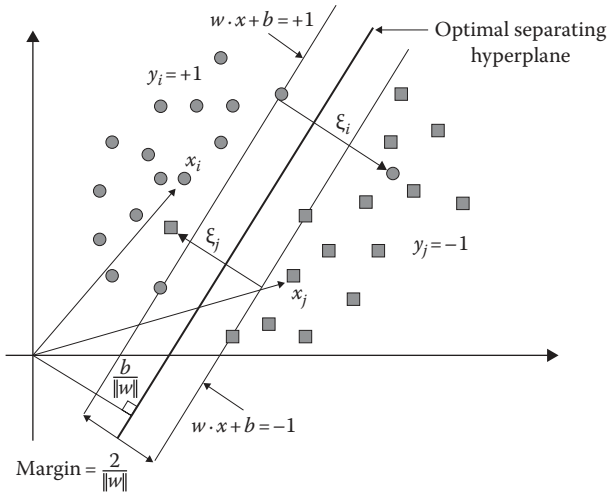

FIGURE 5.1 Classification of a nonlinearly separable case by a SVM.

Recently, innovative kernel-based algorithms with enhanced properties have been developed. These include semisupervised or *transductive* SVMs (TSVMs) learning procedures [16], which are used to exploit both labeled and unlabeled pixels in the training stage, or contextual SVMs [17], in which spatial and spectral information is incorporated by means of the use of proper kernel functions. The capability of semisupervised SVMs to capture the intrinsic information present in the unlabeled data can further mitigate the Hughes phenomenon, and contextual SVMs can address the issues related to the nonstationary behavior of the spectral signatures of classes in the spatial domain.

5.3 SPECTRAL UNMIXING OF HYPERSPECTRAL DATA

Spectral mixture analysis (also called *spectral unmixing*) has been an alluring exploitation goal from the earliest days of hyperspectral imaging [1] to the present [18]. No matter what the spatial resolution is, the spectral signatures collected in natural environments are invariably a mixture of the signatures of the various materials found within the spatial extent of the ground instantaneous field view of the imaging instrument [7]. The availability of hyperspectral imagers with a number of spectral bands that exceeds the number of spectral mixture components [2] has cast the unmixing problem in terms of an over-determined system of equations in which, given a set of pure spectral signatures (called *endmembers*) the actual unmixing to determine apparent pixel *abundance fractions* can be defined in terms of a numerical inversion process.

A standard technique for spectral mixture analysis is *linear* spectral unmixing [19], which assumes that the collected spectra at the spectrometer can be expressed in the form of a linear combination of endmembers weighted by their corresponding abundances. It should be noted that the linear mixture model assumes minimal secondary reflections and/or multiple scattering effects in the data collection procedure, and, hence, the measured spectra can be expressed as a linear combination of the spectral signatures of materials present in the mixed pixel (Figure 5.2a).

Although the linear model has practical advantages such as ease of implementation and flexibility in different applications [3], *nonlinear* spectral unmixing may best characterize the resultant mixed spectra for certain endmember distributions, such as those in which the endmember components are randomly distributed throughout the field of view of the instrument [10,20]. In those cases, the mixed spectra collected at the imaging instrument are better described by assuming that part of the source radiation is multiply scattered before being collected at the sensor (Figure 5.2b).

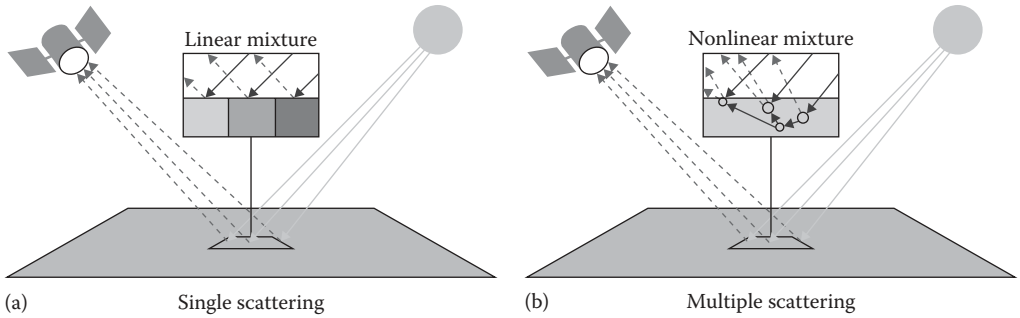

FIGURE 5.2 Graphical interpretation of the linear (a) versus the nonlinear (b) mixture model.

5.3.1 Linear Spectral Unmixing

In order to be able to correctly unmix a hyperspectral data set using the linear model, two requirements are needed:

1. A successful estimation of the number of endmembers (spectrally distinct pure signatures) present in the input hyperspectral scene.
2. The correct determination of a set of endmembers and their correspondent abundance fractions at each pixel.

In order to address the first requirement, two successful techniques in the literature have been the virtual dimensionality (VD) [21] and HySime [22]. The VD concept formulates the issue of whether a distinct signature is present or not in each of the spectral bands as a binary hypothesis testing problem, where a so-called Neyman–Pearson detector is generated to serve as a decision-maker based on a prescribed false alarm probability. In light of this interpretation, the issue of determining an appropriate value for the number of endmembers is further simplified and reduced to setting a specific value of the false alarm probability. In turn, the HySime uses a minimum mean squared error-based approach to determine the signal subspace in hyperspectral imagery.

Regarding the second requirement for successful implementation of the linear mixture model, several algorithms have been developed in recent years for automatic or semiautomatic extraction of spectral endmembers [6]. Classic techniques include the pixel purity index (PPI) [23], N-FINDR [24–26], iterative error analysis (IEA) [27], optical real-time adaptive spectral identification system (ORASIS) [28], convex cone analysis (CCA) [29], vertex component analysis (VCA) [30], and an orthogonal subspace projection (OSP) technique in [31]. Other advanced techniques for endmember extraction have been recently proposed, but few of them consider spatial adjacency. However, one of the distinguishing properties of hyperspectral data is the multivariate information coupled with a two-dimensional (pictorial) representation amenable to image interpretation.

Subsequently, most endmember extraction algorithms listed earlier could benefit from an integrated framework in which both the spectral information and the spatial arrangement of pixel vectors are taken into account. An example is given in Figure 5.3, in which a hyperspectral data cube collected over an urban area (high spatial correlation) is modified by randomly permuting the spatial coordinates of the pixel vectors (i.e., removing the spatial correlation). In both scenes, the application of a spectral-based processing method would yield the same analysis results, while it is clear that a spatial–spectral technique could incorporate the spatial information present in the original scene into the process.

To the best of our knowledge, only a few attempts exist in the literature aimed at including the spatial information in the process of extracting spectral endmembers. Extended morphological operations [13] have been used as a baseline to develop an automatic morphological endmember

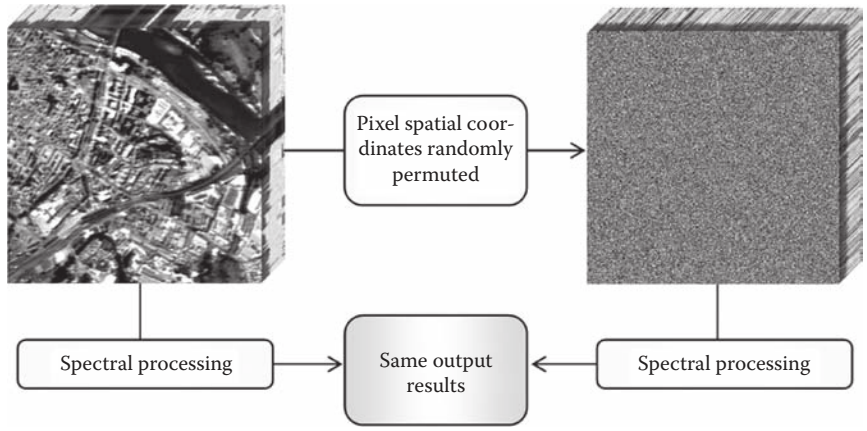

FIGURE 5.3 The importance of including spatial information in hyperspectral data processing.

extraction (AMEE) algorithm [32] for spatial–spectral endmember extraction. Also, spatial averaging of spectrally similar endmember candidates found via singular value decomposition (SVD) was used in the development of the spatial spectral endmember extraction (SSEE) algorithm [33].

Recently, a spatial preprocessing (SPP) algorithm [34] has been proposed. A spatially derived factor is used by this technique to weight the importance of the spectral information associated to each pixel in terms of its spatial context. The SPP is intended as a preprocessing module that can be used in combination with an existing spectral-based endmember extraction algorithm.

Once a set of endmembers have been extracted, their corresponding abundance fractions in a specific pixel vector of the scene can be estimated (in least squares sense) by using the unconstrained and constrained techniques [35]. It should be noted that the fractional abundance estimations obtained in unconstrained fashion do not satisfy the abundance sum-to-one (ASC) and the abundance nonnegativity (ANC) constraints that should hold in order for the linear mixture model to be physically meaningful (i.e., the derived endmember set should be complete and negative abundance estimations lack physical interpretation). Imposing the ASC and ANC constraints leads to a more complex optimization problem, which has been solved (in least-squares sense) in the literature [36].

5.3.2 Nonlinear Spectral Unmixing

In a nonlinear model, the interaction between the *endmembers* and their associated *fractional abundances* is given by a nonlinear function, which is not known a priori. Various machine learning techniques have been proposed in the literature to estimate this function. In particular, artificial neural networks have demonstrated great potential to decompose mixed pixels due to their inherent capacity to approximate complex functions [37]. Although many neural network architectures exist, for decomposition of mixed pixels in terms of nonlinear relationships mostly feed-forward networks of various layers, such as the multilayer perceptron (MLP), have been used [10,38,39]. It has been shown in the literature that MLP-based neural models, when trained accordingly, generally outperform other nonlinear models such as regression trees or fuzzy classifiers [40].

A variety of issues have been investigated in order to evaluate the impact of training in mixed pixel classification accuracy, including the size and location of training sites, and the composition of training sets, but most of the attention has been paid to the issue of training set size, that is, the number of training samples required for the learning stage [41]. Sometimes the smallness of a training set represents a major problem. This is especially apparent for analyses using hyperspectral sensor data, where the requirement of large volumes of training sites is a serious limitation [42].

Even if the endmembers participating in mixtures in a certain area are known, proportions of these endmembers on a per-pixel basis are difficult to be estimated a priori. Therefore, one of the

most challenging aspects in the design of neural network-based techniques for spectral mixture analysis is to reduce the need for very large training sets. Studies have investigated a range of issues [43], including the use of feature selection and feature extraction methods to reduce the dimensionality of the input data [38], the use of unlabeled and semilabeled samples [42], the accommodation of spatial dependence in the data to define an efficient sampling design [33], or the use of statistics derived on other locations [44].

Our speculation (and that of many thoughtful investigators over the past 40 years [42,43]) is that the problem of mixed pixel interpretation demands intelligent training sample selection algorithms, able to seek for the most informative training samples, thus optimizing the compromise between estimation accuracy (to be maximized) and ground-truth knowledge (to be minimized). In this sense, several efforts in the literature have been oriented toward the selection of mixed (border) training samples using previous work developed by Foody, as well as core (pure) training samples developed by simple *endmember* extraction algorithms.

In our experience, machine learning techniques such as MLP neural networks or SVMs can produce stable results when trained accordingly, a fact that leads us to believe that training can indeed be more important than the choice of a specific network architecture in mixture analysis applications.

5.4 EXPERIMENTAL RESULTS

5.4.1 Analysis of Supervised Hyperspectral Data Classification Using SVMs

The hyperspectral scene used for experiments in this subsection was gathered by AVIRIS over the Indian Pines test site in Northwestern Indiana, a mixed agricultural/forested area, early in the growing season, and consists of 1939 × 677 pixels and 204 spectral bands in the wavelength range 400–2500 nm (523 MB in size). Twenty AVIRIS bands (151–170) were removed from the original scene prior to analysis due to low signal-to-noise ratio (SNR) in those bands. The AVIRIS Indian Pines data set represents a very challenging classification problem dominated by similar spectral classes and mixed pixels. Specifically, the primary crops of the area, mainly corn and soybeans, were very early in their growth cycle with only about 5% canopy cover. This fact makes most of the scene pixels highly mixed in nature. Discriminating among the major crops under this circumstances can be very difficult, a fact that has made this scene an extensively used benchmark to validate classification accuracy of hyperspectral imaging algorithms. For illustrative purposes, Figure 5.4a shows a randomly selected spectral band (587 nm) of the original scene and Figure 5.4b shows the corresponding ground-truth map, displayed in the form of a class assignment for each labeled pixel, with 30 mutually exclusive ground-truth classes. Part of these data, including the ground-truth, are available online from Purdue University (from http://dynamo.ecn.purdue.edu/~biehl/MultiSpec).

In the following, three types of kernels are used in experiments: polynomial, Gaussian, and spectral angle mapper. Small training sets, composed of 1%, 2%, 4%, 6%, 8%, 10%, and 20% of the ground-truth pixels available per class, were extracted using pure (core) and mixed (border) training sample selection algorithms [10], and also using a random selection procedure. The SVM was trained with each of these training subsets and then evaluated with the remaining test set. Each experiment was repeated five times in order to guarantee statistical significance, and the mean accuracy values were reported. Table 5.1 summarizes the overall classification results obtained using the three considered kernels and training sample selection algorithms.

From Table 5.1, it can be seen that SVMs generalize quite well: with only 1% of training pixels per class, almost 90% overall classification accuracy is reached by all kernels when trained using border training samples. In all cases, classification accuracies decreased when random and pure samples were used for the training site. This confirms the fact that kernel-based methods in general and SVMs in particular are less affected by the Hughes phenomenon. It is also clear from Table 5.1 that the classification accuracy is generally correlated with the training set size.

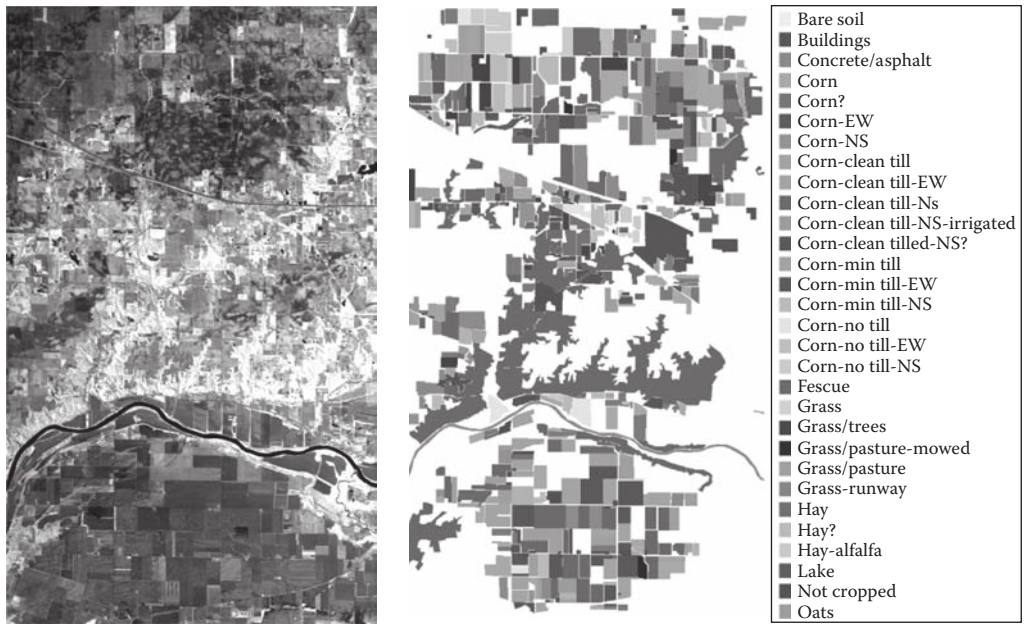

(a) (b)

FIGURE 5.4 (See color insert.) (a) Spectral band at 587 nm wavelength of an AVIRIS scene comprising agricultural and forest features at Indian Pines region. (b) Ground-truth map with 30 mutually exclusive land-cover classes.

TABLE 5.1
Overall Classification Accuracies (in Percentage) Achieved by the SVM Classifier after Applying Polynomial, Gaussian and Spectral Angle Mapper Kernels to the AVIRIS Indian Pines Data Set, Using Different Strategies for Training Sample Selection (Random, Pure, Border Patterns)

Kernel	Training	1%	2%	4%	6%	8%	10%	20%
Polynomial kernel	Random	82.33	82.94	83.21	83.82	85.34	86.12	86.52
	Pure	81.23	82.06	82.80	83.00	84.03	84.45	85.57
	Border	83.44	84.23	84.45	84.96	86.27	87.44	89.96
Gaussian kernel	Random	87.94	88.23	88.78	88.96	89.45	89.48	90.77
	Pure	86.53	87.02	87.64	87.93	88.12	88.26	88.55
	Border	89.45	90.25	91.24	92.08	92.93	93.04	93.67
Spectral angle kernel	Random	85.90	86.22	86.49	87.03	87.56	88.09	88.72
	Pure	85.12	85.67	86.08	86.45	86.97	87.13	87.81
	Border	86.05	86.93	87.57	88.12	89.30	90.12	90.57

However, when border training samples were used, higher classification accuracies were achieved with less training samples. The aforementioned results indicate the importance of including mixed pixels at the border of class boundaries in the training set, as these border patterns are most efficient to determine the hyperplane between two classes.

Finally, it can be seen in Table 5.1 that the best classification scores were generally achieved for the Gaussian kernel, in which the overall accuracy obtained with 1% of the training pixels per class is only 4.22% lower than the overall accuracy obtained with 20% of the training pixels per class

(extracted using border training sample selection). On the other hand, the spectral angle mapper kernel gives slightly degraded classification results. However, with accuracies above 85% in a challenging classification problem, this kernel also provides promising results. Finally, the polynomial kernel needs more training samples than the two other kernels to perform appropriately, as can be seen from the relatively poor results obtained by this kernel for a very limited number of training samples.

5.4.2 Analysis of Unsupervised Linear Unmixing of Hyperspectral Data

The hyperspectral scene used for experiments is the well-known AVIRIS Cuprite data set, available online in reflectance units (from http://aviris.jpl.nasa.gov/html/aviris.freedata.html) after atmospheric correction. This scene has been widely used to validate the performance of endmember extraction algorithms. The portion used in experiments corresponds to a 350 × 350-pixel subset of the sector labeled as f970619t01p02_r02_sc03.a.rfl in the online data. The scene (displayed in Figure 5.5a) comprises 224 spectral bands between 400 and 2500 nm, with full width at half maximum of 10 nm and spatial resolution of 20 m per pixel.

Prior to the analysis, several bands (1–3, 150–170, and 217–224) were removed due to water absorption and low SNR in those bands, leaving a total of 192 reflectance channels to be used in the experiments. The Cuprite site is well understood mineralogically [45,46], and has several exposed minerals of interest included in a spectral library compiled by the U.S. Geological Survey (USGS) available online (from http://speclab.cr.usgs.gov/spectral-lib.html). A few selected spectra from the USGS library, corresponding to several highly representative minerals in the Cuprite mining district (Figure 5.5b), are used in this work to substantiate endmember signature purity.

Two different metrics have been used to compare the performance of endmember extraction and spectral unmixing algorithms in the AVIRIS Cuprite scene. The first metric is the spectral angle [3,19] between each extracted endmember and the set of available USGS ground-truth spectral signatures. Low spectral angle scores mean high spectral similarity between the compared vectors. This spectral similarity measure is invariant in the multiplication of pixel vectors by constants and, consequently, is invariant before unknown multiplicative scalings that may arise due to differences in illumination and angular orientation. In our experiments, the spectral angle allows us to identify the USGS signature that is most similar to each endmember

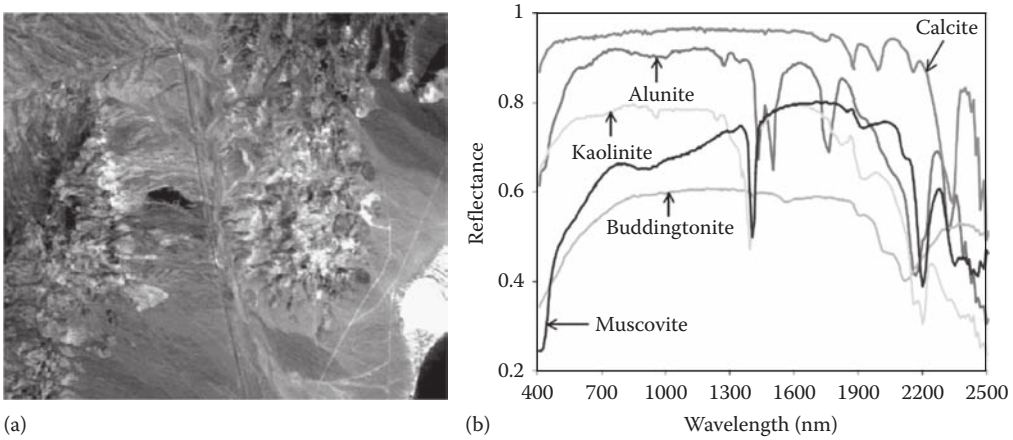

FIGURE 5.5 (a) False color composition of the remote sensing image used in experiments. (b) Reference spectral signatures provided by USGS and used for validation purposes.

automatically extracted from the scene by observing the minimum spectral angle reported for such endmember across the entire set of USGS signatures.

A second metric employed to evaluate the goodness of the reconstruction is the root mean square error (RMSE) obtained in the reconstruction of the hyperspectral image (using the derived endmembers and their corresponding abundance fractions). This metric is based on the assumption that a set of high-quality endmembers (and their corresponding estimated abundance fractions) may allow reconstruction of the original hyperspectral scene with higher precision than a set of low-quality endmembers. In this case, the original hyperspectral image is used to measure the fidelity of the reconstructed version of the same scene on a per-pixel basis.

Table 5.2 tabulates the spectral angles (in degrees) obtained after comparing the USGS library spectra of five highly representative minerals in the Cuprite mining district (alunite, buddingtonite, calcite, kaolinite, and muscovite) with the corresponding endmembers extracted by several different algorithms (listed in subsection 5.3.1) from the AVIRIS Cuprite scene. In all cases, the input parameters of the different endmember extraction methods tested have been carefully optimized so that the best performance for each method is reported. Again, the smaller the spectral angles across the five minerals in Table 5.2, the better the results. It should be noted that Table 5.2 only displays the smallest spectral angle scores of all endmembers with respect to each USGS signature for each algorithm.

For reference, the mean spectral angle values across all five USGS signatures are also reported. In all cases, the number of endmembers to be extracted was set to 14 after using a consensus between the VD concept and the HySime method. Table 5.2 reveals that the AMEE provides very good results (all spectral angle values scores below 10°), with the SSEE and the SPP + OSP (where SPP indicates spatial preprocessing prior to the classic OSP procedure for endmember extraction) are the algorithms that can provide comparable—but slightly worst—results. Table 5.2 also reveals that, in this real example, SPP generally improves the signature purity of the endmembers extracted by spectral-based algorithms.

On the other hand, Figure 5.6 graphically represents the per-pixel RMSE obtained after reconstructing the AVIRIS Cuprite scene using 14 endmembers extracted by different methods. It can be seen that the methods using SPP (SPP + OSP, SPP + N-FINDR, SPP + VCA) improve their respective spectral-based versions in terms of the quality of image reconstruction, while both AMEE and SSEE also provide lower reconstruction errors than OSP, N-FINDR, and VCA. These results suggest the advantages of incorporating spatial information into the automatic extraction of image endmembers from the viewpoint of obtaining more spatially representative spectral signatures, which can be used to describe other mixed signatures in the scene.

TABLE 5.2
Spectral Angle Scores (in Degrees) between the USGS Mineral Spectra and Their Corresponding Endmember Pixels Produced by Several Endmember Extraction Algorithms

Algorithm	Alunite	Buddingtonite	Calcite	Kaolinite	Muscovite	Mean
OSP	4.81	4.16	9.62	11.14	5.41	7.03
N-FINDR	9.96	7.71	12.08	13.27	5.24	9.65
VCA	10.73	9.04	6.36	14.05	5.41	9.12
SPP + OSP	4.95	4.16	9.96	10.90	4.62	6.92
SPP + N-FINDR	12.81	8.33	9.83	10.43	5.28	9.34
SPP + VCA	12.42	4.04	9.37	7.37	6.18	7.98
AMEE	4.81	4.21	9.54	8.74	4.61	6.38
SSEE	4.81	4.16	8.48	11.14	4.62	6.64

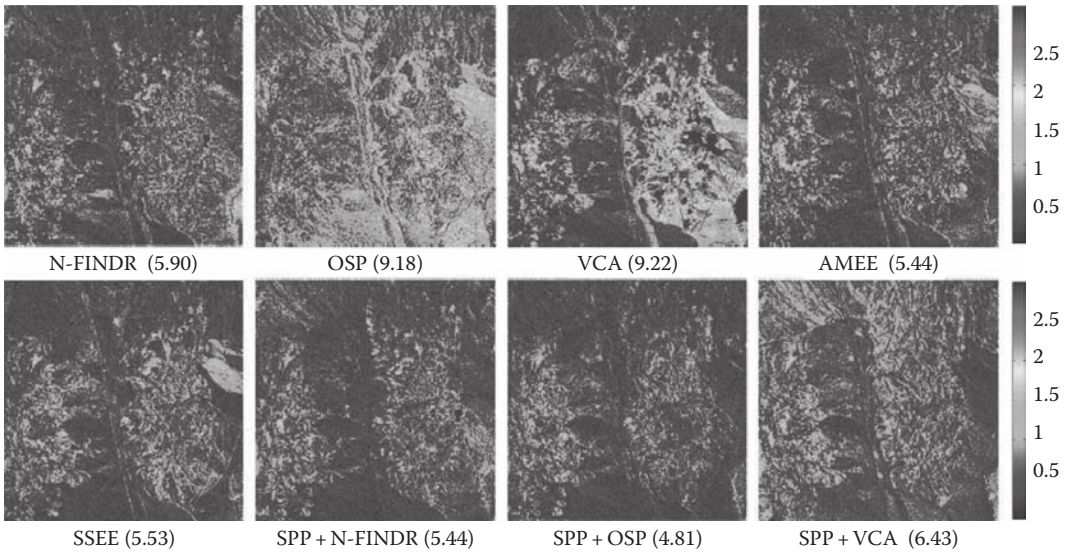

FIGURE 5.6 **(See color insert.)** RMSE reconstruction errors (in percentage) for various endmember extraction algorithms after reconstructing the AVIRIS Cuprite scene.

5.4.3 Analysis of Supervised Nonlinear Unmixing of Hyperspectral Data Using MLPs

In the Iberian Peninsula, Dehesa systems are used for a combination of livestock, forest, and agriculture activity [47]. The outputs of these systems include meat, milk, wool, charcoal, cork bark, and grain. Around 12%–18% of the area is harvested on a yearly basis. The crops are used for animal feed or for cash cropping, depending on the rainfall of the area. Determination of fractional land-cover using remote sensing techniques may allow for a better monitoring of natural resources in Dehesa agro-ecosystems.

Our choice of this type of landscape for evaluating nonlinear unmixing techniques was made on several accounts. The first one is the availability of hyperspectral image data sets with accurate geo-registration for a real Dehesa test site in Caceres, SW Spain, collected simultaneously in July 2001 by two instruments operating at multiple spatial resolutions: Digital Airborne Imaging Spectrometer (DAIS) 7915 and Reflective Optics Spectrographic Imaging System (ROSIS), operated by the German Aerospace Agency (DLR). A second major reason is the simplicity of the Dehesa landscape, which greatly facilitates the collection of reliable field data for model validation purposes. It is also important to emphasize that the scenes were collected in summertime, so atmospheric interferers were greatly minimized. Before describing our experiments, we first provide a comprehensive description of the data sets used and ground-truth activities in the study area.

The data used in this study consisted of two main components: image data and field measurements of land-cover fractions, collected at the time of image data acquisition. The image data are formed by a ROSIS scene collected at high spatial resolution, with 1.2 m pixels, and its corresponding DAIS 7915 scene, collected at low spatial resolution with 6 m pixels. The spectral range from 504 to 864 nm (consisting of a total of 112 spectral bands) was selected for experiments, not only because it is adequate for analyzing the spectral properties of the landscape under study, but also because this spectral range is well covered by the two considered sensors through narrow spectral bands. Figure 5.7 shows the full flightline of the ROSIS scene, which comprises a Dehesa area located between the facilities of University of Extremadura in Caceres (leftmost part of the flightline) and Guadiloba water reservoir at the center of the flightline. Figure 5.8a shows the Dehesa test site selected for experiments, which corresponds to a highly representative Dehesa area that

FIGURE 5.7 Flightline of a ROSIS hyperspectral scene collected over a Dehesa area in Caceres, Spain.

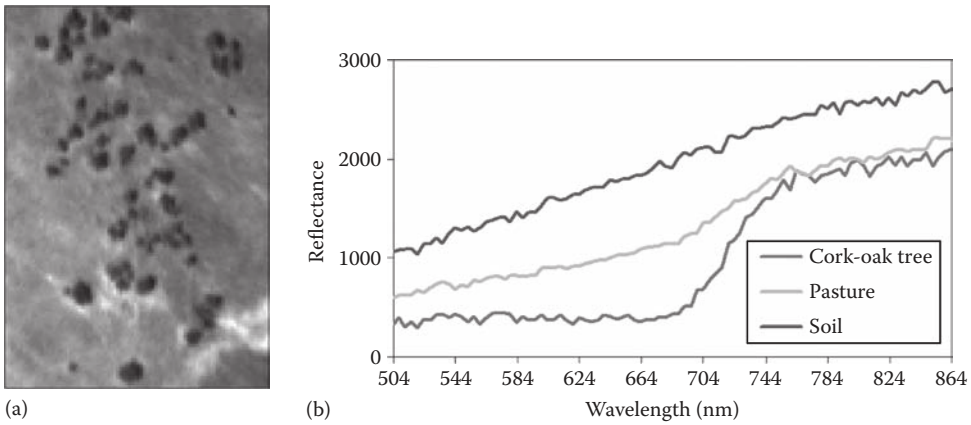

FIGURE 5.8 **(See color insert.)** (a) Spectral band (584 nm) of a ROSIS Dehesa subset selected for experiments. (b) Endmember signatures of soil, pasture, and cork-oak tree extracted by the AMEE algorithm, where scaled reflectance values are multiplied by a constant factor.

contains several cork-oak trees (appearing as dark spots) and several pasture (gray) areas on a bare soil (white) background. Several field techniques were applied to obtain reliable estimates of the fractional land cover for each DAIS 7915 pixel in the considered Dehesa test site:

1. First, the ROSIS image was roughly classified into the three land-cover components discussed earlier using a maximum-likelihood supervised classification approach based on image-derived spectral endmembers, where Figure 5.8b shows the three endmembers used for mapping that were derived using the AMEE algorithm. Our assumption was that the pixels in the ROSIS image were sufficiently small to become spectrally simple to analyze.
2. Then, the classified ROSIS image was registered with the DAIS 7915 image using a ground control point-based method with subpixel accuracy [48].
3. The classification map was then associated with the DAIS 7915 image to provide an initial estimation of land cover classes for each pixel at the DAIS 7915 image scale. For that purpose, a 6×6 m grid was overlaid on the 1.2×1.2 m classification map derived from the ROSIS scene, where the geographic coordinates of each pixel center point were used to validate the registration with subpixel precision.
4. Next, fractional abundances were calculated within each 6×6 m grid as the proportion or ROSIS pixels labeled as cork-oak tree, pasture, and soil located within that grid, respectively.

(a) (b) (c)

FIGURE 5.9 Ground measurements in the Dehesa area of study located in Caceres, Spain. (a) Spectral sample collection using an ASD FieldSpec Pro spectroradiometer. (b) High-precision GPS geographic delimitation. (c) Field spectral measurements at different altitudes.

5. Most importantly, the abundance maps at the ROSIS level were thoroughly refined using field measurements (Figure 5.9a) before obtaining the final proportions. Several approaches were developed to refine the initial estimations:
   a. Fractional land cover data were collected on the ground at more than 30 evenly distributed field sites within the test area. These sites were delineated during the field visit as polygons, using high-precision global positioning system (GPS) coordinates (see Figure 5.9b).
   b. Land cover fractions were estimated at each site using a combination of various techniques. For instance, field spectra were collected for several areas using an Analytical Spectral Devices (ASD) FieldSpec Pro spectro-radiometer. Of particular interest were field measurements collected on top of tree crowns (Figure 5.9c), which allowed us to model different levels of tree crown transparency.
   c. On the other hand, the early growth stage of pasture during the summer season allowed us to perform ground estimations of pasture abundance in selected sites of known dimensions, using pasture harvest procedures supported by visual inspection and laboratory analyses.

After following the aforementioned sequence of steps, we obtained a set of approximate fractional abundance labels for each pixel vector in the DAIS 7915 image. Despite our effort to conduct a reliable ground estimation of fractional land-cover in the considered semiarid environment, absolute accuracy is not claimed. We must emphasize, however, that the combined use of imagery data at different resolutions, subpixel ground control-based image registration, and extensive field work including high-precision GPS field work, spectral sample data collection, and expert knowledge represents a novel contribution in the area of spectral mixture analysis validation, in particular, for Dehesa-type ecosystems.

In order to evaluate the accuracy of linear spectral in the considered application, Figure 5.10 shows the scatter plots of measured versus linearly estimated fractional abundances (using linear spectral unmixing with the ASC and ANC constraints imposed) for the three considered land-cover materials in the DAIS 7915 (low spatial resolution) image data set, where the diagonal represents perfect match and the two flanking lines represent plus/minus 20% error bound. Here, the three spectral endmembers were derived using the AMEE algorithm, which incorporates spatial information into the endmember extraction process.

As expected, the flatness of the test site largely removed topographic influences in the remotely sensed response of soil areas. As a result, most linear predictions for the soil endmember fall within the 20% error bound (see Figure 5.10a). On the other hand, the multiple scattering within the pasture and cork-oak tree canopies (and from the underlying surface in the latter case) complicated the spectral mixing in nonlinear fashion, which resulted in a generally higher number of estimations lying

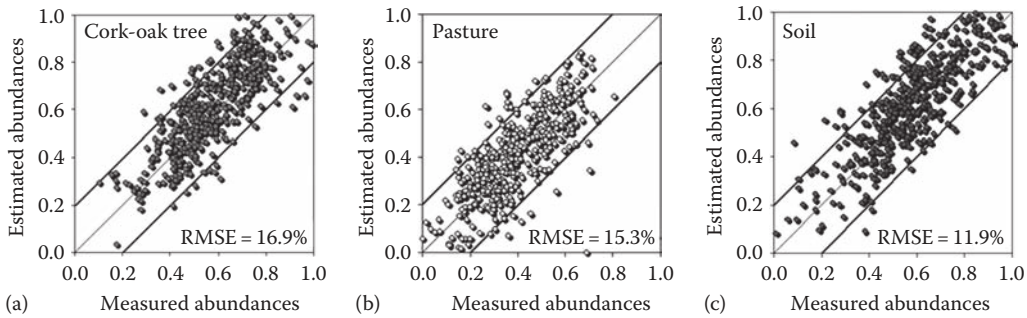

FIGURE 5.10 Abundance estimations of cork-oak tree (a), pasture (b), and soil (c) by the fully constrained linear mixture model from the DAIS 7915 image.

outside the error bound, as illustrated in Figures 5.10b and c. Also, the RMSE scores in abundance estimation for the soil (11.9%), pasture (15.3%), and cork-oak tree (16.9%) were all >10% estimation error in percentage, which suggested that linear mixture modeling was not flexible enough to accommodate the full range of spectral variability throughout the landscape.

In order to characterize the Dehesa ecosystem structure better than linear models do, we used nonlinear spectral unmixing to better characterize nonlinear mixing effects. For this purpose, we applied a mixed (border) training sample selection algorithm to automatically locate highly descriptive training sites in the DAIS 7915 scene and then used the obtained samples (and the ground-truth information associated to those samples) to train the MLP-based neural network model described in subsection 5.3.2. Figure 5.11 shows the scatter plots of measured versus predicted fractional abundances for soil, pasture, and cork-oak tree by the proposed MLP-based model, first trained with the three pure training samples by the AMEE algorithm (Figure 5.11b) plus 40 additional training samples selected by an algorithm designed to seek for the most highly mixed training samples [10]. This represents <1% of the total number of pixels in the DAIS 7915 scene. These samples were excluded from the testing set made up of all remaining pixels in the scene. From Figure 5.11, it is clear that the utilization of intelligently selected training samples resulted in fewer points outside the two 20% difference lines, most notably, for both pasture and cork-oak abundance estimates.

The pattern of the scatter plots obtained for the soil predictions (Figure 5.11a) was similar (in particular, when the soil abundance was high). Most importantly, the RMSE scores in abundance estimation were significantly reduced (with regard to the experiment using fully constrained linear unmixing) for the soil (6.1%), pasture (4%), and cork-oak tree (6.3%). These results confirm our intuition that nonlinear effects in Dehesa landscapes mainly result from multiple scattering effects in vegetation canopies. It is worth noting that, although the ASC and ANC constraints were not imposed in our proposed MLP-based learning stage, negative and/or unrealistic abundance

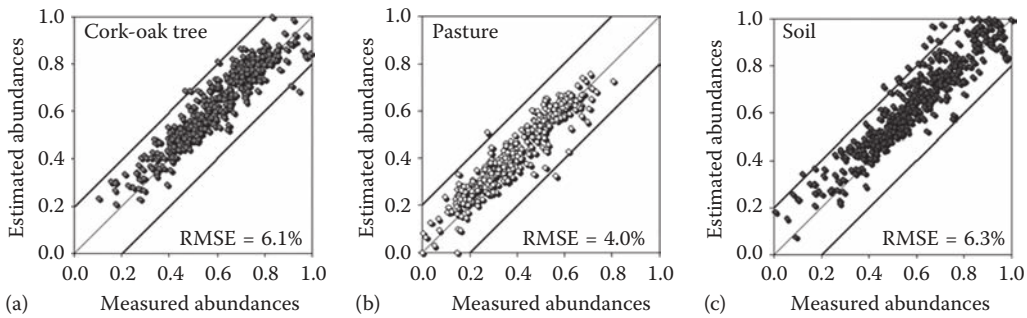

FIGURE 5.11 Abundance estimations of cork-oak tree (a), pasture (b), and soil (c) by the MLP-based mixture model, trained using mixed (border) samples, from the DAIS 7915 image.

estimations (which usually indicate a bad fit of the model and reveal inappropriate endmember/training data selection) were very rarely found in our experiments.

The experimental validation carried out in this subsection indicates that the intelligent incorporation of mixed training samples can enable a more accurate representation of nonlinearly mixed signatures. It was apparent from experimental results that the proposed neural network-based model was able to generate abundance estimates that were close to abundance values measured in the field, using only a few intelligently generated training samples. The need for mixed training data does, however, require detailed knowledge on abundance fractions for the considered training sites. In practice, these data are likely to be derived from imagery acquired at a finer spatial resolution than the imagery to be classified, for example, using data sets acquired by sensors operating simultaneously at multiple spatial resolutions as it is the case of the DAIS 7915 and ROSIS instruments considered in this experiment. Such multiresolution studies may also incorporate prior knowledge or ancillary information, which can be used to help target the location of training sites, and to focus training site selection activities on regions likely to contain the most informative training samples.

5.5 CONCLUSIONS AND FUTURE PERSPECTIVES

This chapter focused on hyperspectral data processing algorithms that included (a) SVM techniques for supervised classification using limited training samples and (b) development of linear and nonlinear spectral unmixing techniques, some of them integrating the spatial and the spectral information. The special characteristics of hyperspectral images pose new processing problems, not to be found in other types of remotely sensed data:

1. The high-dimensional nature of hyperspectral data introduces important limitations in supervised, full-pixel classifiers, such as the limited availability of training samples or the inherently complex structure of the data (leading to the Hughes phenomenon).
2. There is a need to integrate the spatial and spectral information to take advantage of the complementarities that both sources of information can provide, in particular, for unsupervised mixed-pixel classifiers.

In this regard, the SVM experiments reported in our quantitative assessment demonstrated that, with only 1% of training pixels per class, almost 90% overall classification accuracy is reached by all kernels when trained using border training samples. This highlighted the opportunity of overcoming the Hughes phenomenon using kernel approaches. On the other hand, our unmixing experiments indicate that new trends in algorithm design (such as the joint use of spatial and spectral information in linear spectral unmixing, or the development of nonlinear unmixing models based on machine learning techniques with an appropriate exploitation of limited training samples) can significantly improve the accuracy in the estimation of fractional abundances in real analysis scenarios.

As demonstrated by our experimental results and the determination of the accuracy of these approaches, techniques are rapidly changing from *hard* classifiers to soft classifiers. In this regard, we anticipate that the full adaptation of *soft* classifiers to mixed-pixel classification problems (e.g., via multiregression and robust training sample selection algorithms) may push the frontiers of hyperspectral data classification to new application domains. Further developments on the joint exploitation of the spatial and the spectral information in the input data are also needed to complement initial approximations to the problem of interpreting the data in unsupervised fashion, thus being able to cope with the dramatically enhanced spatial and spectral capabilities expected in the design of future imaging spectrometers. Advances in high performance computing [49], including clusters of computers and distributed grids, as well as specialized hardware modules such as field programmable gate arrays (FPGAs) or graphics processing units (GPUs), will also be crucial to help increase algorithm efficiency and meet timeliness needs in many remote sensing applications.

ACKNOWLEDGMENT

This work has been supported by the European Community's Marie Curie Research Training Networks Programme under reference MRTN-CT-2006-035927, Hyperspectral Imaging Network (HYPER-I-NET). This work has also been supported by the Spanish Ministry of Science and Innovation (HYPERCOMP/EODIX project, reference AYA2008-05965-C04-02). Gabriel Martín and Sergio Sánchez are sponsored by research fellowships with references BES-2009-017737 and PTA2009-2611-P, respectively, both associated to the aforementioned project. Funding from Junta de Extremadura (local government) under project PRI09A110 is also gratefully acknowledged. The authors thank Andreas Mueller for his lead of the DLR project that allowed us to obtain the DAIS 7915 and ROSIS hyperspectral datasets over Dehesa areas in Extremadura, Spain; David Landgrebe at Purdue University for making the AVIRIS Indian Pines scene available to the scientific community, and Robert O. Green at NASA/JPL for also making the AVIRIS Cuprite scene available to the scientific community. Last but not least, the authors would like to take this opportunity to gratefully acknowledge the editors of this volume for their very kind invitation to contribute a chapter and for all their support and encouragement during the different stages of the production process for this monograph.

REFERENCES

1. A. F. H. Goetz, G. Vane, J. E. Solomon, and B. N. Rock, Imaging spectrometry for Earth remote sensing, *Science*, 228, 1147–1153, 1985.
2. R. O. Green, Imaging spectroscopy and the airborne visible-infrared imaging spectrometer (AVIRIS), *Remote Sensing of Environment*, 65, 227–248, 1998.
3. C.-I. Chang, *Hyperspectral Imaging: Techniques for Spectral Detection and Classification*, Kluwer Academic and Plenum Publishers, New York, 2003.
4. D. A. Landgrebe, *Signal Theory Methods in Multispectral Remote Sensing*, John Wiley & Sons, Hoboken, NJ, 2003.
5. J. A. Richards, Analysis of remotely sensed data: The formative decades and the future, *IEEE Transactions on Geoscience and Remote Sensing*, 43, 422–432, 2005.
6. A. Plaza, P. Martinez, R. Perez, and J. Plaza, A quantitative and comparative analysis of endmember extraction algorithms from hyperspectral data, *IEEE Transactions on Geoscience and Remote Sensing*, 42, 650–663, 2004.
7. J. B. Adams, M. O. Smith, and P. E. Johnson, Spectral mixture modeling: A new analysis of rock and soil types at the Viking Lander 1 site, *Journal of Geophysical Research*, 91, 8098–8112, 1986.
8. G. M. Foody and A. Mathur, Toward intelligent training of supervised image classifications: Directing training data acquisition for SVM classification, *Remote Sensing of Environment*, 93, 107–117, 2004.
9. A. Plaza, J. A. Benediktsson, J. Boardman, J. Brazile, L. Bruzzone, G. Camps-Valls, J. Chanussot et al., Recent advances in techniques for hyperspectral image processing, *Remote Sensing of Environment*, 113, 110–122, 2009.
10. J. Plaza, A. Plaza, R. Perez, and P. Martinez, On the use of small training sets for neural network-based characterization of mixed pixels in remotely sensed hyperspectral images, *Pattern Recognition*, 42, 3032–3045, 2009.
11. P. Gamba, F. Dell'Acqua, A. Ferrari, J. A. Palmason, and J. A. Benediktsson, Exploiting spectral and spatial information in hyperspectral urban data with high resolution, *IEEE Geoscience and Remote Sensing Letters*, 1, 322–326, 2004.
12. J. A. Benediktsson, J. A. Palmason, and J. R. Sveinsson, Classification of hyperspectral data from urban areas based on extended morphological profiles, *IEEE Transactions on Geoscience and Remote Sensing*, 42, 480–491, 2005.
13. A. Plaza, P. Martinez, J. Plaza, and R. Perez, Dimensionality reduction and classification of hyperspectral image data using sequences of extended morphological transformations, *IEEE Transactions on Geoscience and Remote Sensing*, 43(3), 466–479, 2005.
14. G. Camps-Valls and L. Bruzzone, Kernel-based methods for hyperspectral image classification, *IEEE Transactions on Geoscience and Remote Sensing*, 43, 1351–1362, 2005.
15. K. R. Muller, S. Mika, G. Ratsch, K. Tsuda, and B. Scholkopf, An introduction to kernel-based learning algorithms, *IEEE Transactions on Neural Networks*, 12, 181–202, 2001.

16. L. Bruzzone, M. Chi, and M. Marconcini, A novel transductive SVM for the semisupervised classification of remote sensing images, *IEEE Transactions on Geoscience and Remote Sensing*, 44, 3363–3373, 2006.
17. G. Camps-Valls, L. Gomez-Chova, J. Munoz-Mari, J. Vila-Frances, and J. Calpe-Maravilla, Composite kernels for hyperspectral image classification, *IEEE Geoscience and Remote Sensing Letters*, 3, 93–97, 2006.
18. M. E. Schaepman, S. L. Ustin, A. Plaza, T. H. Painter, J. Verrelst, and S. Liang, Earth system science related imaging spectroscopy—An assessment, *Remote Sensing of Environment*, 113, 123–137, 2009.
19. N. Keshava and J. F. Mustard, Spectral unmixing, *IEEE Signal Processing Magazine*, 19, 44–57, 2002.
20. K. J. Guilfoyle, M. L. Althouse, and C.-I. Chang, A quantitative and comparative analysis of linear and nonlinear spectral mixture models using radial basis function neural networks, *IEEE Transactions on Geoscience and Remote Sensing*, 39, 2314–2318, 2001.
21. C.-I. Chang and Q. Du, Estimation of number of spectrally distinct signal sources in hyperspectral imagery, *IEEE Transactions on Geoscience and Remote Sensing*, 42, 608–619, 2004.
22. J. M. Bioucas-Dias and J. M. P. Nascimento, Hyperspectral subspace identification, *IEEE Transactions on Geoscience and Remote Sensing*, 46, 2435–2445, 2008.
23. J. W. Boardman, F. A. Kruse, and R. O. Green, Mapping target signatures via partial unmixing of AVIRIS data, *Proceedings JPL Airborne Earth Science Workshop*, JPL Publication, Washington, DC, pp. 23–26, 1995.
24. M. E. Winter, N-FINDR: An algorithm for fast autonomous spectral endmember determination in hyperspectral data, *Proceedings of SPIE*, Vol. 3753, pp. 266–277, 1999.
25. M. E. Winter, A proof of the N-FINDR algorithm for the automated detection of endmembers in a hyperspectral image, *Proceedings of SPIE Algorithms and Technologies for Multispectral, Hyperspectral, and Ultraspectral Imagery X*, Vol. 5425, pp. 31–41, 2004.
26. M. Zortea and A. Plaza, A quantitative and comparative analysis of different implementations of N-FINDR: A fast endmember extraction algorithm, *IEEE Geoscience and Remote Sensing Letters*, 6, 787–791, 2009.
27. R. A. Neville, K. Staenz, T. Szeredi, J. Lefebvre, and P. Hauff, Automatic endmember extraction from hyperspectral data for mineral exploration, *Proceedings of 21st Canadian Symposium on Remote Sensing*, Ottawa, Ontario, Canada, pp. 21–24, 1999.
28. J. H. Bowles, P. J. Palmadesso, J. A. Antoniades, M. M. Baumback, and L. J. Rickard, Use of filter vectors in hyperspectral data analysis, *Proceedings of SPIE Infrared Spaceborne Remote Sensing III*, Vol. 2553, pp. 148–157, 1995.
29. A. Ifarraguerri and C.-I. Chang, Multispectral and hyperspectral image analysis with convex cones, *IEEE Transactions on Geoscience and Remote Sensing*, 37(2), 756–770, 1999.
30. J. M. P. Nascimento and J. M. Bioucas-Dias, Vertex component analysis: A fast algorithm to unmix hyperspectral data, *IEEE Transactions on Geoscience and Remote Sensing*, 43(4), 898–910, 2005.
31. J. C. Harsanyi and C.-I. Chang, Hyperspectral image classification and dimensionality reduction: An orthogonal subspace projection, *IEEE Transactions on Geoscience and Remote Sensing*, 32(4), 779–785, 1994.
32. A. Plaza, P. Martinez, R. Perez, and J. Plaza, Spatial/spectral endmember extraction by multidimensional morphological operations, *IEEE Transactions on Geoscience and Remote Sensing*, 40, 2025–2041, 2002.
33. D. M. Rogge, B. Rivard, J. Zhang, A. Sanchez, J. Harris, and J. Feng, Integration of spatial–spectral information for the improved extraction of endmembers, *Remote Sensing of Environment*, 110, 287–303, 2007.
34. M. Zortea and A. Plaza, Spatial preprocessing for endmember extraction, *IEEE Transactions on Geoscience and Remote Sensing*, 47, 2679–2693, 2009.
35. D. Heinz and C.-I. Chang, Fully constrained least squares linear mixture analysis for material quantification in hyperspectral imagery, *IEEE Transactions on Geoscience and Remote Sensing*, 39, 529–545, 2001.
36. C.-I. Chang and D. Heinz, Constrained subpixel target detection for remotely sensed imagery, *IEEE Transactions on Geoscience and Remote Sensing*, 38, 1144–1159, 2000.
37. C. M. Bishop, *Neural Networks for Pattern Recognition*, Oxford University Press, Oxford, U.K., 1995.
38. J. Plaza and A. Plaza, Spectral mixture analysis of hyperspectral scenes using intelligently selected training samples, *IEEE Geoscience and Remote Sensing Letters*, 7, 371–375, 2010.
39. A. Baraldi, E. Binaghi, P. Blonda, P. A. Brivio, and P. Rampini, Comparison of the multilayer perceptron with neuro-fuzzy techniques in the estimation of cover class mixture in remotely sensed data, *IEEE Transactions on Geoscience and Remote Sensing*, 39, 994–1005, 2001.
40. W. Liu and E. Y. Wu, Comparison of non-linear mixture models, *Remote Sensing of Environment*, 18, 1976–2003, 2004.
41. X. Zhuang, B. A. Engel, D. F. Lozano, R. B. Fernndez, and C. J. Johannsen, Optimization of training data required for neuro-classification, *International Journal of Remote Sensing*, 15, 3271–3277, 1999.

AQ1

42. M. Chi and L. Bruzzone, A semilabeled-sample-driven bagging technique for ill-posed classification problems, *IEEE Geoscience and Remote Sensing Letters*, 2, 69–73, 2005.
43. G. M. Foody, The significance of border training patterns in classification by a feedforward neural network using back propagation learning, *International Journal of Remote Sensing*, 20, 3549–3562, 1999.
44. C. C. Borel and S. A. W. Gerslt, Nonlinear spectral mixing models for vegetative and soil surfaces, *Remote Sensing of Environment*, 47, 403–416, 1994.
45. R. N. Clark, G. A. Swayze, K. E. Livo, R. F. Kokaly, S. J. Sutley, J. B. Dalton, R. R. McDougal, and C. A. Gent, Imaging spectroscopy: Earth and planetary remote sensing with the USGS Tetracorder and expert systems, *Journal of Geophysical Research*, 108, 1–44, 2003.
46. G. Swayze, R. N. Clark, F. Kruse, S. Sutley, and A. Gallagher, Ground-truthing AVIRIS mineral mapping at Cuprite, Nevada, *Proceedings of the JPL Airborne Earth Science Workshop*, JPL Publication, Washington, DC, pp. 47–49, 1992.
47. F. J. Pulido, M. Diaz, and S. J. Hidalgo, Size structure and regeneration of Spanish holm oak Quercus ilex forests and dehesas: Effects of agroforestry use on their long-term sustainability, *Forest Ecology and Management*, 146, 1–13, 2001.
48. A. Plaza, J. L. Moigne, and N. S. Netanyahu, Morphological feature extraction for automatic registration of multispectral scenes, *Proceedings of the IEEE International Geoscience and Remote Sensing Symposium*, Vol. 1, pp. 421–424, 2007.
49. A. Plaza and C.-I. Chang, *High Performance Computing in Remote Sensing*, CRC Press, Boca Raton, FL, 2007.

AUTHOR QUERY

[AQ1] Please provide the location of the proceedings for the references [24,25,28,48].